STRUCTURAL CHEMISTRY

ISSN 2053-2296

Experimental and theoretical investigations on a furan-2-carboxamide-bearing thiazole: synthesis, molecular characterization by IR/NMR/XRD, electronic characterization by DFT, Hirshfeld surface analysis and biological activity

Şükriye Çakmak,[a]* Başak Koşar Kırca,[b] Aysel Veyisoğlu,[a] Hasan Yakan,[c] Cem Cüneyt Ersanlı[d] and Halil Kütük[e]

[a]Department of Medical Services and Techniques, Vocational School of Health Services, Sinop University, Sinop, Turkey, [b]Department of Mathematics and Science Education, Sinop University, Sinop, Turkey, [c]Department of Chemistry Education, Ondokuz Mayis University, Samsun, Turkey, [d]Department of Physics, Faculty of Arts and Sciences, Sinop University, Sinop, Turkey, and [e]Department of Chemistry, Faculty of Arts and Sciences, Ondokuz Mayis University, Samsun, Turkey. *Correspondence e-mail: scakmak@sinop.edu.tr

Received 1 January 2022
Accepted 21 February 2022

Edited by M. Rosales-Hoz, Cinvestav, Mexico

Keywords: thiazolamide; antimicrobial activity; spectroscopic evaluation; biological activity; furan; carboxamide; XRD; Hirshfeld surface; crystal structure.

CCDC reference: 2085414

Supporting information: this article has supporting information at journals.iucr.org/c

A thiazole-based heterocyclic amide, namely, *N*-(thiazol-2-yl)furan-2-carboxamide, $C_8H_6N_2O_2S$, was synthesized and investigated for its antimicrobial activity. The structure was characterized by elemental analysis and IR, ^{1}H NMR, and ^{13}C NMR spectroscopy. The molecular and electronic structures were investigated experimentally by single-crystal X-ray diffraction (XRD) and theoretically by density functional theory (DFT) modelling. The compound crystallized in the monoclinic space group $P2_1/n$ and the asymmetric unit contains two symmetrically independent molecules. Several noncovalent interactions were recorded by XRD and analysed with Hirshfeld surface analysis (HSA) calculations. Natural bond orbital, molecular electrostatic potential, second-order nonlinear optical and thermodynamic property analyses were also carried out using the DFT/B3LYP method. The title compound was evaluated for antimicrobial activity against eight microorganisms consisting of Gram-negative bacteria, Gram-positive bacteria and fungi. The compound showed good antimicrobial activity against the eight tested microorganisms. This suggests that the compound merits further study for potential pharmacological and medical applications.

1. Introduction

The class of thiazole-ring-bearing compounds is one of the most extensively studied classes of aromatic five-membered heterocycles. They contain nitrogen and sulfur heteroatoms, and play an important role in medicinal chemistry due to their extensive applications, such as antibacterial (Mishra *et al.*, 2020; Srivastava *et al.*, 2019), antifungal (Meleddu *et al.*, 2016), anticancer (Gomha *et al.*, 2016; Ramos-Inza *et al.*, 2019; Sharma *et al.*, 2020), anti-inflammatory (Araniciu *et al.*, 2014; Rödl *et al.*, 2014), anti-HIV (Venkatachalam *et al.*, 2001), antimalarial (Bueno *et al.*, 2016), anti-oxidant (Jaishree *et al.*, 2012; Bhaskara Reddy *et al.*, 2015; Geronikaki *et al.*, 2013), analgesic (Siddiqui *et al.*, 2019; Kumar & Singh, 2021), anti-convulsant (Mishchenko *et al.*, 2020), antidiabetic (Gao *et al.*, 2016; Wang *et al.*, 2018) and antihypertensive (El-Enany *et al.*, 2020). The thiazole nucleus is an essential unit present in many natural molecules, such as thiamin (known as vitamin B1), which play a vital role in human life (Chhabria *et al.*, 2016). It is also found in penicillin and various commercial synthetic drugs. The thiazole moiety appears in essential dyes and

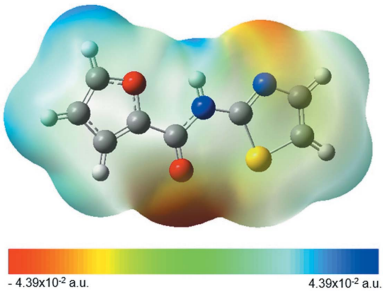

several agricultural pesticides (Weng *et al.*, 2013; Kaur Gill *et al.*, 2018).

In recent years, studies in the field of antimicrobial drugs have focused on the discovery of new agents with antibacterial activity in order to overcome the rapid development of drug resistance (Borcea *et al.*, 2021).

Based on the above information and considering the need to discover and develop active agents, a thiazole amide derivative was synthesized, namely, *N*-(thiazol-2-yl)furan-2-carboxamide (**1**). The synthesized compound was characterized *via* spectroscopic methods, X-ray crystal structure analysis and electronic structure analysis. Furthermore, the antibacterial and antifungal activities of **1** were investigated.

This study aims also to provide theoretical information, such as electronic properties, natural bond orbital analysis, molecular electrostatic potential, thermodynamic and nonlinear optical parameters, about **1** using the B3LYP method with the 6-311G(d,p) basis set.

2. Experimental

2.1. Instrumentation

All chemicals were purchased from commercial sources (Merck, ABCR or Sigma–Aldrich) and were used without further purification. The tetrahydrofuran (THF) solvent was of analytical grade. The melting point of **1** was recorded with a Stuart SMP 30 apparatus and is uncorrected. IR spectra were taken on a Bruker Vertex 80V. ^{1}H and ^{13}C NMR spectra were recorded on a Bruker/Ultraschilt operating at 300 MHz for ^{1}H and at 75 MHz for ^{13}C NMR in $CDCl_3$. Elemental analysis wwas carried out on an Elementar Vario Micro Cube (Germany) elemental analyzer at ODUMARAL in Ordu University.

2.2. Synthesis and crystallization

Thiazol-2-amine (15 mmol) was dissolved in THF (7.5 ml) and trimethylamine (2.1 ml, 15 mmol) was added dropwise. At room temperature, a solution of 2-furoyl chloride (2.55 g, 12 mmol) in THF (7.5 ml) was added slowly to the reaction mixture. After the reaction mixture had been stirred at room temperature for 12 h, the resulting white salt precipitate was filtered off and water (150 ml) was added to the filtrate. The precipitate was filtered off and washed three times with water to remove excess amine and triethylamine hydrochloride. The crude product was crystallized from acetonitrile–methanol (2:1 *v*/*v*). The synthesis reaction is shown in Scheme 1. The synthetic procedure was a slightly modified version of that reported by Mazik *et al.* (1999).

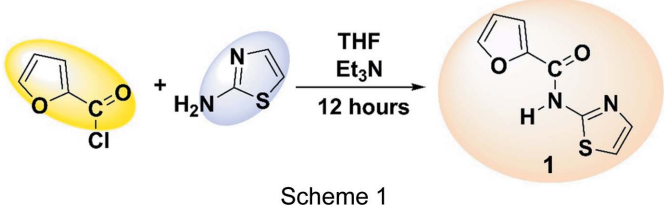

Scheme 1

Table 1
Experimental details.

Crystal data	
Chemical formula	$C_8H_6N_2O_2S$
M_r	194.21
Crystal system, space group	Monoclinic, $P2_1/n$
Temperature (K)	296
a, b, c (Å)	11.9532 (11), 11.1161 (10), 13.4093 (12)
β (°)	104.071 (3)
V (Å^3)	1728.3 (3)
Z	8
Radiation type	Mo $K\alpha$
μ (mm^{-1})	0.34
Crystal size (mm)	0.17 × 0.12 × 0.11
Data collection	
Diffractometer	Bruker APEXII CCD
No. of measured, independent and observed [$I > 2\sigma(I)$] reflections	44822, 4276, 3424
R_{int}	0.035
(sin $\theta/\lambda)_{max}$ (Å^{-1})	0.667
Refinement	
$R[F^2 > 2\sigma(F^2)]$, $wR(F^2)$, S	0.045, 0.134, 0.94
No. of reflections	4276
No. of parameters	241
H-atom treatment	H atoms treated by a mixture of independent and constrained refinement
$\Delta\rho_{max}$, $\Delta\rho_{min}$ (e Å^{-3})	0.41, −0.33

Computer programs: *APEX3* (Bruker, 2013), *SAINT* (Bruker, 2013), *SHELXS2013* (Sheldrick, 2008), *SHELXL2013* (Sheldrick, 2015), *Mercury* (Macrae *et al.*, 2020) and *WinGX* (Farrugia, 2012).

Analytical data: light-yellow–cream; yield 1.68 g, 72%; literature yield 74%; m.p. 149–152 °C; analysis calculated (%) for $C_8H_6N_2O_2S$: C 49.47, H 3.11, N 14.42, S 16.51; found: C 49.57, H 3.10, N 14.43, S 16.62.

2.3. Refinement

Crystal data, data collection and structure refinement details are summarized in Table 1. All H atoms, except for H2*A* and H4, were positioned geometrically and refined using a riding model. The C—H bond lengths were fixed at 0.93 Å and the U_{iso} values of the H atoms were fixed at 1.2 times the U_{eq} value of the parent atoms.

2.4. Antimicrobial activity studies

Eight microorganisms (*Bacillus subtilis* ATCC 6623, *Staphylococcus aureus* ATCC 25923, *Enterococcus faecalis* ATCC 29212, *Escherichia coli* ATCC 25922, *Klebsiella pneumoniae* ATCC 70060, *Pseudomonas aeruginosa* ATCC 27853, *Candida albicans* ATCC 10231 and *Aspergillus niger* ATCC 16404) were used for the antimicrobial activity analysis. Compound **1** was dissolved in dimethyl sulfoxide (DMSO) at the proper concentration. Three of the microorganisms are Gram-positive bacteria (*Bacillus subtilis* ATCC 6623, *Staphylococcus aureus* ATCC 25923 and *Enterococcus faecalis* ATCC 29212), three are Gram-negative bacteria (*Escherichia coli* ATCC 25922, *Klebsiella pneumoniae* ATCC 70060 and *Pseudomonas aeruginosa* ATCC 27853) and two are fungi (*Candida albicans* ATCC 10231 and *Aspergillus niger* ATCC

16404). The antimicrobial activity study was performed using the microdilution method (Schwalbe *et al.*, 2007) by the broth microdilution method carried out in 96-well microplates. The cultures were obtained from nutrient broth for all the bacterial strains after 24 h of incubation at 37 °C. Fungi were maintained in the nutrient broth after incubation for 24 h at 28 °C. Bacterial and fungi cells were homogenized in the nutrient broth. The turbidity of bacterial and fungi suspensions was set at a concentration of approximately 10^6 cells ml^{-1}. DMSO, pure microorganisms and pure media were used as control wells. A 100 µl suspension of each microorganism and a 100 µl suspension of **1** were added to the wells. The microplate with no growth of microorganism was recorded to represent the minimum inhibitory concentration (MIC) in µg ml^{-1}. Amoxicillin and tetracycline were used as the reference standards for antibacterial activity, while ketoconazole was used as the reference standard for antifungal activity.

Table 2
Dihedral angles (°) between planes **P1**, **P2** and **P3**.

See Fig. 2 for definitions of the planes.

Molecule	**P1–P2**	**P2–P3**	**P1–P3**
A	4.44	5.96	9.04
B	3.86	4.12	6.64

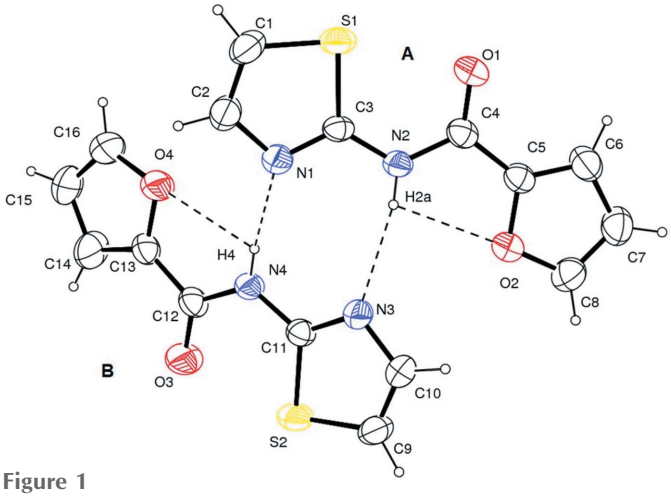

Figure 1
Atom-numbering scheme of **1**. The dashed bonds indicate the intramolecular hydrogen bonds and the hydrogen bonds in the asymmetric unit. H atoms are drawn as small spheres of arbitrary radii and the other atoms are shown as displacement ellipsoids at the 30% probability level.

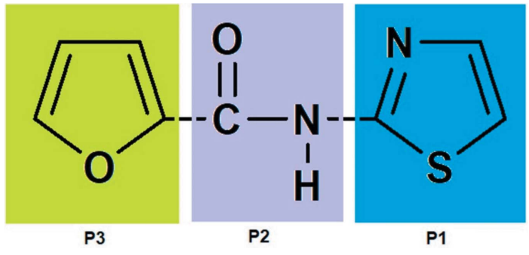

Figure 2
The **P1**, **P2** and **P3** planes of **1**.

Table 3
Geometric details (Å, °) of the noncovalent interactions for **1**.

*Cg*1 is the centroid of the S1/C1/C2/N1/C3 ring, *Cg*2 is the centroid of the O2/C5/C6/C7/C8 ring, *Cg*3 is the centroid of the S2/C9/C10/N3/C11 ring and *Cg*4 is the centroid of the O4/C13–C16 ring. α is the dihedral angle between planes *CgI* and *CgJ*, β is the angle between the *CgI*–*CgJ* vector and normal to plane *I*, and γ is the angle between the *CgI*–*CgJ* vector and the normal to plane *J*.

D—H···*A*	*D*—H	H···*A*	*D*···*A*	*D*—H···*A*
N2—H2*A*···O2	0.81 (2)	2.41	2.738 (3)	106
N4—H4···O4	0.80 (3)	2.47	2.763 (3)	103
N2—H2*A*···N3	0.81 (2)	2.23	3.023 (3)	164
N4—H4···N1	0.80 (3)	2.14	2.926 (3)	168
C8—H8···O3^{i}	0.93	2.42	3.300 (3)	159

X—H···*Cg*	*X*—H	H···*Cg*	*X*···*Cg*	*X*—H···*Cg*
C7—H7···*Cg*1^{ii}	0.93	2.86	3.621 (3)	140

Cg···*Cg*	*Cg*···*Cg*	α	β	γ
*Cg*1···*Cg*2^{iii}	3.782 (3)	9	15.7	24.2
*Cg*2···*Cg*1^{iii}	3.782 (3)	9	24.2	15.7
*Cg*3···*Cg*4^{iv}	3.890 (4)	7	22.7	16.3
*Cg*4···*Cg*3^{iv}	3.890 (4)	7	16.3	22.7

Symmetry codes: (i) $-x+\frac{3}{2}, y-\frac{1}{2}, -z+\frac{1}{2}$; (ii) $x+\frac{1}{2}, -y+\frac{1}{2}, z+\frac{1}{2}$; (iii) $-x+1, -y+1, -z+1$; (iv) $-x+1, -y+1, -z$.

3. Results and discussion

3.1. Crystal structure

Compound **1** crystallized in the monoclinic space group $P2_1/n$ and the asymmetric unit contains two crystallographically independent molecules denoted **A** and **B**. Fig. 1 (Farrugia, 2012) shows the molecular structure with the atom-numbering scheme.

The molecular geometries of molecules *A* and *B* are almost planar, and the dihedral angles between the planar groups which form the molecular structure, *i.e.* **P1**, **P2** and **P3** (see

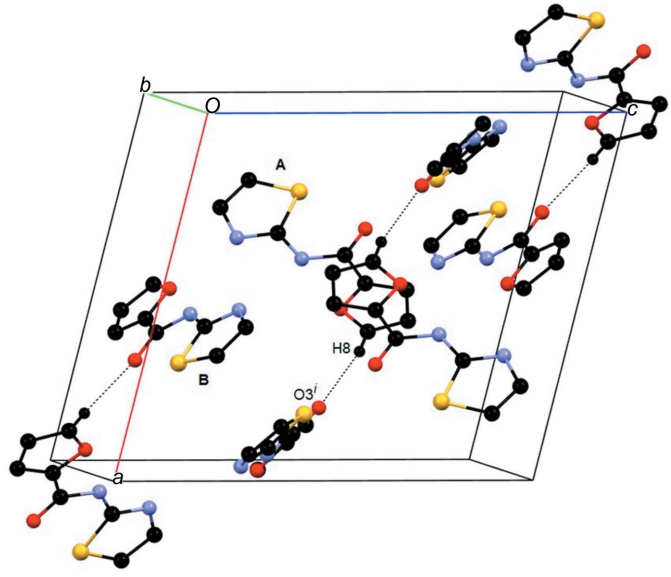

Figure 3
Part of the crystal structure of **1**, showing the intermolecular C—H···O hydrogen bonds parallel to the *ac* plane of the unit cell. For clarity, H atoms not involved in the motifs have been omitted.

Table 4
Selected geometrical parameters (Å, °).

A		*B*	
C4═O1	1.224 (2)	C12═O3	1.226 (3)
C4—N2	1.372 (3)	C12—N4	1.362 (2)
N2—C3	1.377 (3)	N4—C11	1.383 (3)
C4—C5	1.454 (3)	C12—C13	1.458 (3)
C3—S1	1.731 (2)	C11—S2	1.725 (2)
C1—S1	1.721 (3)	C9—S1	1.719 (3)
N1—C3—N2—C4	179.6 (2)	N3—C11—N4—C12	175.2 (2)
C3—N2—C4—C5	176.9 (2)	C11—N4—C12—C13	−176.3 (2)
N2—C4—C5—C6	174.3 (2)	N4—C12—–C13—C14	176.5 (3)

Fig. 2), are listed in Table 2. The reason for the slight differences between the dihedral angles and thus the planarity of the two molecules in the asymmetric unit can be explained by the different environments formed by these two molecules during crystallization.

There is another factor which affects molecular conformation: noncovalent interactions are highly effective in determining molecular conformation, due to the repulsive and attractive forces they create, as well as in crystal formation in three dimensions. The crystal structure of **1** displays an intermolecular hydrogen bond, a C—H···π interaction, four π–π interactions and weak van der Waals interactions in the three-dimensional (3D) network. The geometric details of these noncovalent interactions are listed in Table 3 with the relevant symmetry codes.

The crystal packing of **1** is stabilized by two intramolecular N—H···O hydrogen bonds, two N—H···N hydrogen bonds in the asymmetric unit, an intermolecular C—H···O hydrogen bond, a C—H···π interaction and four π–π interactions. While the intramolecular N—H···O hydrogen bonds (Fig. 1) form two pseudo-five-membered rings, the N—H···N hydrogen bonds form an $R_2^2(8)$ motif according to graph-set notation and link two independent identical molecules in the asymmetric unit (Etter *et al.*, 1990). The only intermolecular hydrogen bond in the structure is C8—H8···O3^{i} (Fig. 3). Fig. 4

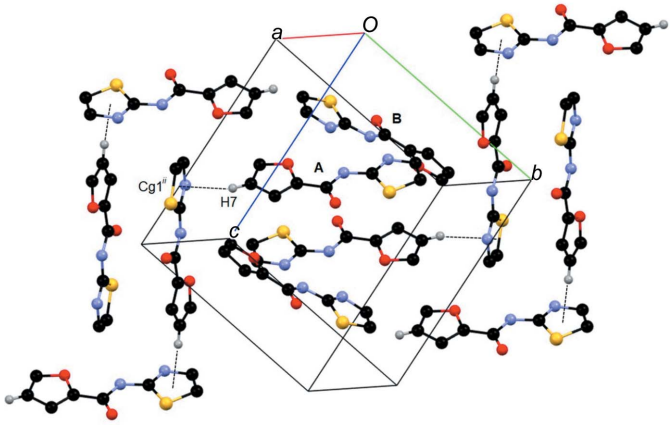

Figure 4
Part of the crystal structure of **1**, showing the C—H···π interactions parallel to the *bc* plane of the unit cell. For clarity, H atoms not involved in the motifs have been omitted.

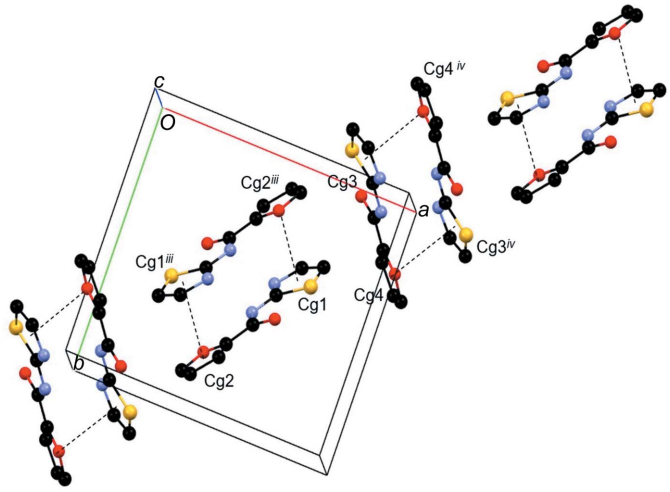

Figure 5
Part of the crystal structure of **1**, showing the π–π interactions parallel to the *ab* plane of the unit cell. For clarity, H atoms not involved in the motifs have been omitted.

shows part of the crystal structure of **1** parallel to the *bc* plane of the unit cell, with the molecules linked by C7—H7···*Cg*1^{ii} interactions (see Table 3 for centroid description). Lastly, the π–π interactions in the crystal structure are shown in Fig. 5.

Table 4 summarizes selected bond lengths and angles for **1**. The C—N and C═O bond lengths in the amide group are in the expected range and are in agreement with similar values in the literature (Koşar Kırca *et al.*, 2018, 2020; Çakmak *et al.*, 2016; Demir *et al.*, 2015; Sonar *et al.*, 2012; Hennig *et al.*, 2009; Prabukanthan *et al.*, 2018).

3.2. Vibrational frequencies

In the IR spectrum of **1**, the symmetric and asymmetric stretching vibrations of the amino group (–NH_2) were not seen at 3500 cm^{-1}, while the –NH stretching vibration of the amide group was observed as a new peak. These results indicate that the reaction was successful and expected. The N—H stretching vibration was observed as a characteristic peak at 3286 cm^{-1}, as expected in the target compound. The –C═O (amide I) stretching vibration was observed as characteristic peaks at 1667 cm^{-1}. The other group wavenumber is the –C—N stretching vibration with an –NH bending vibration (amide II) caused by the Fermi resonance effect. In compound **1**, the mode was observed at 1413 cm^{-1} (Fig. 6). The aromatic –CH stretching vibration was observed at 3096 cm^{-1}. The –C═N, –C—N,
–C—O and –C—S stretching vibrations were observed at 1532, 1324, 1267 and 851 cm^{-1}, respectively. In a previous work, the NH, C═O and C═N stretching vibrations of 2,3-dimethoxy-*N*-(thiazol-2-yl)benzamide were observed at 3221, 1681 and 1554 cm^{-1}, respectively (Yakan *et al.*, 2020). In another study, the N—H and C═O stretching vibrations of 3-acetoxy-2-methyl-*N*-(3-methylphenyl)benzamide were observed at 3234 and 1651 cm^{-1}, respectively (Koşar Kırca *et al.*, 2020). These observations are in agreement with similar compounds

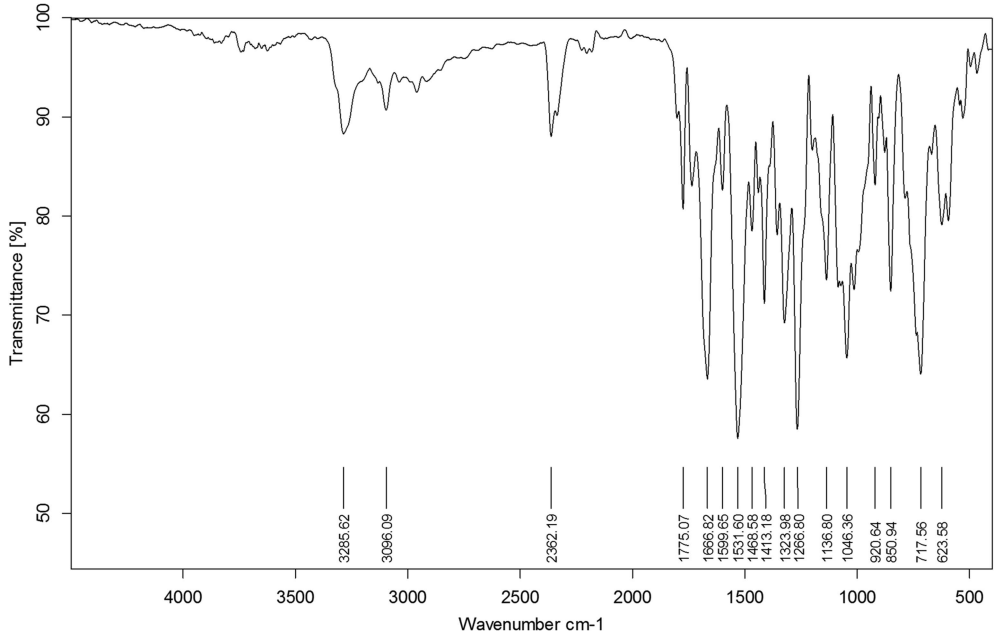

Figure 6
IR spectrum of **1**.

reported previously (Rubio-Pérez *et al.*, 2012; Koşar Kırca *et al.*, 2020; Yakan *et al.*, 2020; Iriarte *et al.*, 2008).

3.3. ^{1}H NMR spectra

The ^{1}H NMR spectrum of **1** was recorded in $CDCl_3$ (7.28 ppm). The signal of the amino proton (N—H) was seen as a broad singlet at 11.82 ppm (*br*, 1H) which is specific for this kind of amide proton. The aromatic protons (H1–H3) of the furan ring were observed at 7.58–6.63 ppm (Fig. 7). The H1 proton coupled to the H2 proton resonated as a doublet peak at 7.58 ppm. The H2 proton coupled to both the H3 and H1 protons resonated as a triplet peak at 6.63 ppm. The H3 proton coupled to the H2 proton resonated as a doublet peak at 7.05 ppm. The aromatic protons (H4 and H5) of the thiazole ring were observed at 7.54–7.37 ppm. The H4 proton coupled to the H5 proton resonated as a doublet peak at 7.54 ppm. The H5 proton coupled to the H4 proton resonated as a doublet peak at 7.37 ppm.

In an earlier study, the N—H proton signals of amides, including heterocyclic, were observed at 11.44, 11.73 and 11.99 ppm. In the same study, the aromatic protons (H4 and H5) of the thiazole ring were observed at 7.53–7.03 ppm (Yakan *et al.*, 2020). These data agree with proton values reported for similar compounds (Koşar Kırca *et al.*, 2020; Yakan *et al.*, 2020; Choi *et al.*, 2014; Kerdphon *et al.*, 2015).

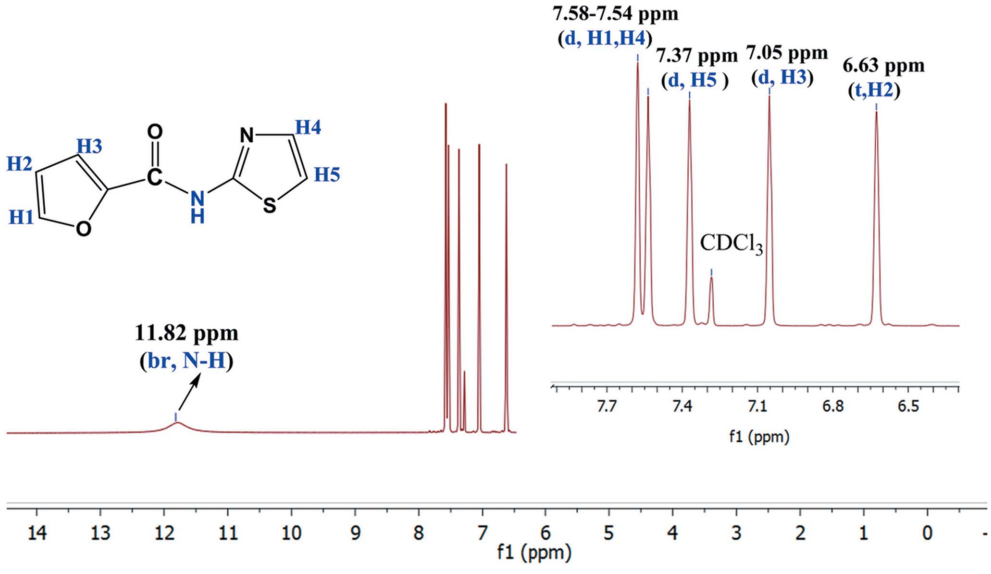

Figure 7
^{1}H spectrum of **1** in $CDCl_3$.

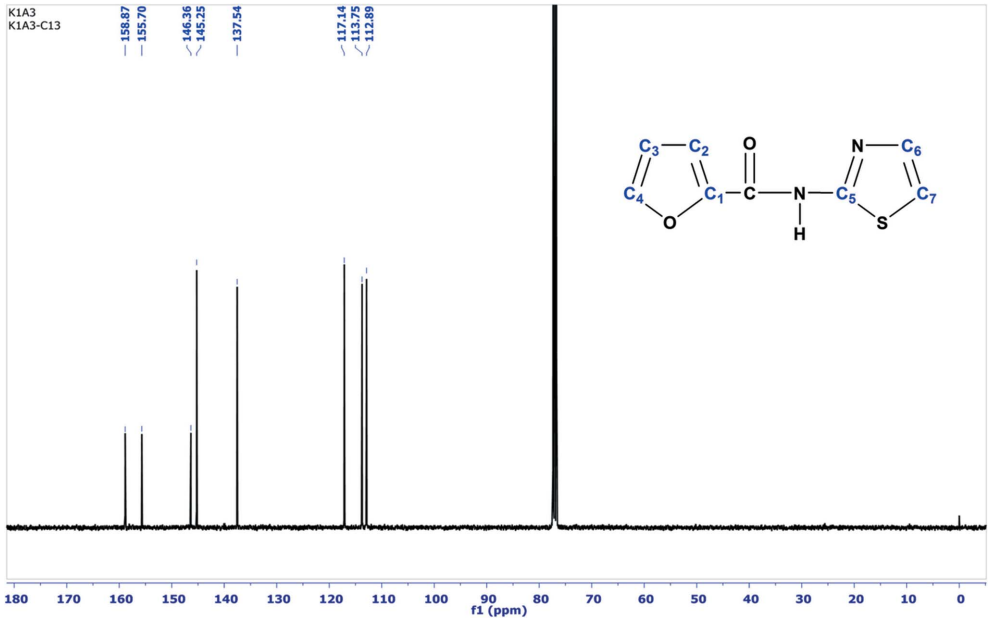

Figure 8
^{13}C spectrum of **1** in $CDCl_3$

3.4. ^{13}C NMR spectra

The ^{13}C NMR spectrum of **1** was recorded in $CDCl_3$ (77 ppm, triplet) and showed eight different resonances, which are in good agreement with the proposed structure shown in Fig. 8. The carbonyl peak (C═O) of the amide group was observed at 158.87 ppm. The –C═N (C5) group and atoms C6 and C7 of the thiazole ring resonate at 155.70, 137.54 and 112.89 ppm, respectively. The C6 atom was shifted downfield (high values of δ) owing to the electronegative N atom. The C1, C2, C3 and C4 atoms of the furan ring were observed at 146.36, 113.75, 117.14 and 145.25 ppm, respectively. The C1 and C4 atoms were shifted downfield on account of the electronegative O atom. In an earlier study, the C═O signals of amide, including heterocyclic, were observed at 162.9–172.5 ppm. In the same study, the C5–C7 atoms of the thiazole ring were observed at 153.1, 138.9 and 130.6 ppm, respectively (Yakan *et al.*, 2020). These results are consistent with values reported for similar compounds (Rubio-Pérez *et al.*, 2012; Yakan *et al.*, 2020; Choi *et al.*, 2014; Kerdphon *et al.*, 2015).

3.5. Hirshfeld surface analysis

Hirshfeld surface analysis is a unique and useful tool for understanding the nature of intermolecular interactions and the 3D packing modes of crystal structures. The Hirshfeld surface can be described as an area around the molecule separating it from the space in the crystal (Spackman & Jayatilaka, 2009; Tojiboev *et al.*, 2020). This analysis allows the creation of several maps, such as d_{norm}, shape index and curvedness, each giving different information, and two-dimensional (2D) fingerprint plots, which show the contributions of noncovalent interactions to the crystal packing in a quantitative manner. Three distinct colours appear on a 3D molecular Hirshfeld surface plotted over d_{norm} for a molecule: red, blue and white. Red corresponds to contacts shorter (with a negative d_{norm} value) than the sum of the van der Waals radii, blue to longer ones (with a positive d_{norm} value) and white corresponds exactly to the sum of the van der Waals radii (with a zero d_{norm} value). The shape index and curvedness maps supply additional information about noncovalent interactions. Blue and red triangles on a shape-index map indicate that the ring atoms of the molecule are inside the surface and the π-stacked molecule above them, while large flat regions described by a blue outline on the curvedness

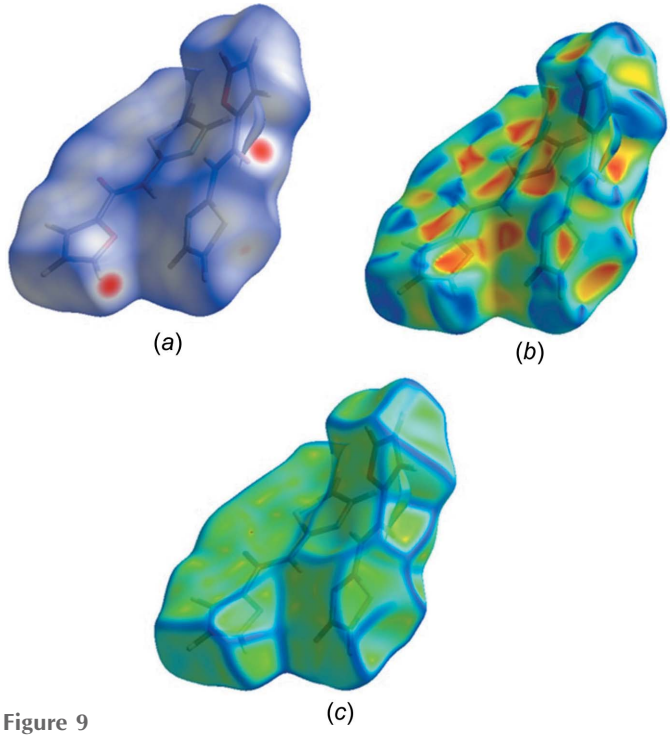

Figure 9
Molecular Hirshfeld surfaces plotted over (*a*) d_{norm}, (*b*) shape index and (*c*) curvedness for **1**.

maps indicate the presence of π–π interactions (Shyamapada *et al.*, 2016).

To perform the Hirshfeld surface analysis, the program *CrystalExplorer* was used with the crystallographic information file (.cif) of the crystal synthesized (Version 21.5; Spackman *et al.*, 2021). Molecular Hirshfeld surfaces plotted over d_{norm}, shape index and curvedness for **1** are shown in Figs. 9(*a*), 9(*b*) and 9(*c*), respectively. The d_{norm} surface map was plotted over the range −0.2105 to 1.2515 a.u., the shape-index map over the range −0.9970 to 0.9982 a.u. and the curvedness map over the range −4.0298 to 0.3226 a.u. The bright-red spots on the d_{norm} map indicate that the primary intermolecular interactions for this molecule are C—H···O hydrogen bonding, as can be appreciated from the data given in Table 3.

While the red and blue triangles on the shape-index surface in Fig. 9(*b*) indicate C—H···π interactions, the evidence for π–π interactions appears as a large flat region on the curvedness map in Fig. 9(*c*).

Fig. 10 shows the 2D fingerprint plots from the Hirshfeld surface analysis of **1** with the relative percentage contributions of the major interactions. H···H contacts have a 25.9% contribution to the overall crystal packing, O···H/H···O 21.7%, C···H/H···C 15.6%, S···H/H···S 11.4%, C···C 7.6% and N···H/H···N 7.5%. The small percentage contributions from the other interatomic interactions to the Hirshfeld surfaces are as follows: C···S/S···C 3.3%, O···S/S···O 2.8%, C···N/N···C 2.2%, C···O/O···C 0.9%, O···N/N···O 0.7% and O···O 0.4%. These interactions can be seen as 'other' in the pie chart at the bottom right corner of Fig. 10. The fingerprint plots of **1** clearly show that the major contributions to the crystal packing are from the H···H, O···H/H···O and C···H/H···C contacts. While the 'wings' shape, which is known to be a characteristic of C—H···π interactions, can be seen in the fingerprint plot in Fig. 10(*d*), the other characteristic is the 'two large spikes' shape in Fig. 10(*g*) and indicates that there are also N···H interactions in the crystal packing.

Table 5
Electron delocalization and second-order interaction energies.

Donor (*i*)	Acceptor (*j*)	$E(2)$ (kcal mol^{-1})	E_j - E_i (a.u.)	F_{ij} (a.u.)
π(C3—N1)	π*(C1—C2)	18.97	0.35	0.075
π(C5—C6)	π*(C4—O1)	19.69	0.29	0.070
π(C5—C6)	π*(C7—C8)	15.74	0.29	0.061
π(C7—C8)	π*(C5—C6)	16.66	0.30	0.066
n1(N1)	σ*(C3—S1)	15.79	0.55	0.084
n2(O1)	σ*(C4—C5)	18.57	0.69	0.104
n2(O1)	σ*(C4—N2)	24.89	0.69	0.119
n2(O2)	π*(C5—C6)	25.36	0.37	0.087
n2(O2)	π*(C7—C8)	26.89	0.36	0.089
n2(S1)	π*(C1—C2)	19.28	0.26	0.066
n2(S1)	π*(C3—N1)	30.93	0.24	0.077
n1(N2)	π*(C3—N1)	42.74	0.27	0.098
n1(N2)	π*(C4—O1)	59.66	0.28	0.116

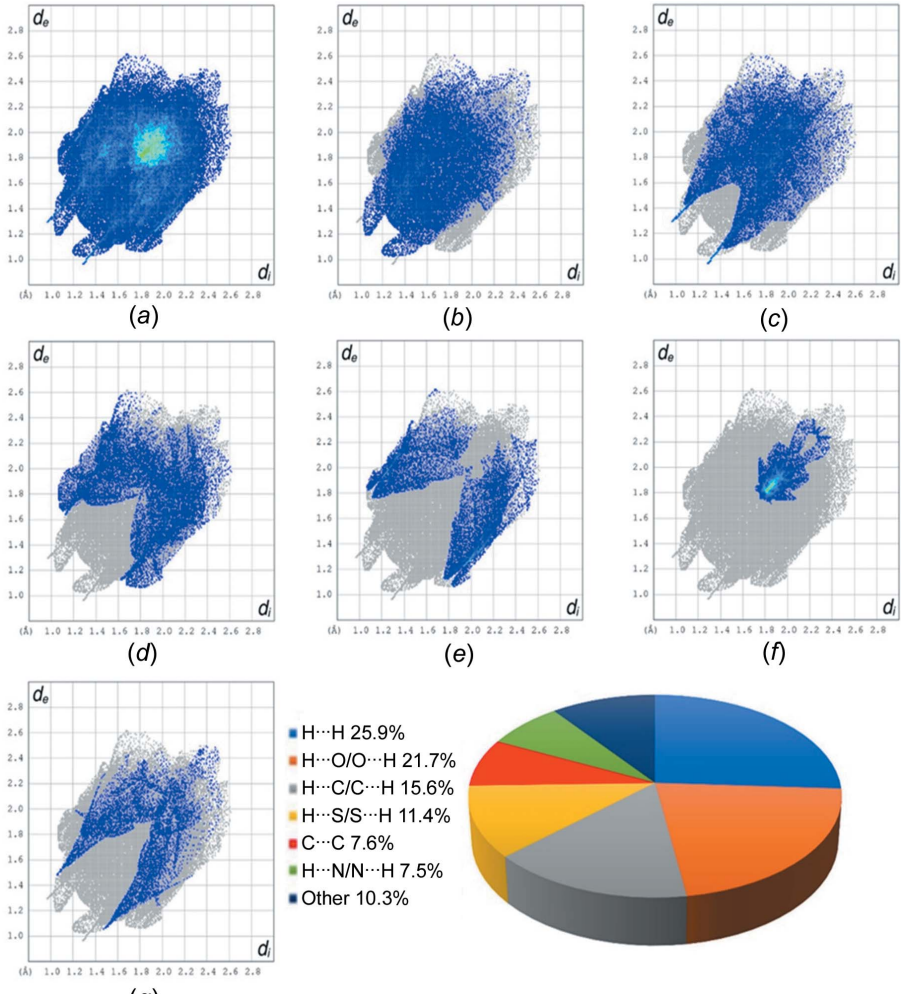

Figure 10
Two-dimensional fingerprint plots for contributions of individual interactions larger than 5%, showing (*a*) all contacts, (*b*) H···H, (*c*) O···H/H···O, (*d*) C···H/H···C, (*e*) S···H/H···S, (*f*) C···C and (*g*) N···H/H···N.

3.6. Electronic structure

For all the density functional theory (DFT) calculations, a B3LYP hybrid exchange-correlation functional (Lee *et al.*, 1988; Becke, 1993) was employed with the 6-311G(d,p) basis set (Ditchfield *et al.*, 1971), as implemented in the *GAUSSIAN03* package (Frisch *et al.*, 2004). All the electronic structure investigations were carried out on the selected *A* molecule in the asymmetric unit starting from the crystallographic coordinates.

3.6.1. Natural bond orbital (NBO) analysis. Hydrogen bonding plays a very important role in protein structures and amides are the repeat units in the backbones of all proteins. Because of the polar character of amides, which results

Table 6
Thermodynamic properties of **1** at different temperatures.

Temperature (K)	Enthalpy (kcal mol^{-1})	Entropy (cal mol^{-1} K)	Heat capacity (cal mol^{-1} K)
100	1.317	74.019	17.003
150	2.364	82.618	21.891
200	3.745	90.256	27.646
250	5.376	97.539	33.939
300	7.321	104.651	40.266
350	9.580	111.622	46.282
400	12.153	118.434	51.801
450	14.977	125.061	56.754
500	17.980	131.482	61.147

from electron delocalization, these groups form relatively strong hydrogen bonds using the C═O group and the N—H proton. The electronic delocalization and electrostatic potential surfaces have been investigated based on a natural bond orbital (NBO) analysis and a molecular electrostatic potential (MEP) plot of **1** with the help of DFT in this part of the study.

The NBO calculations, a common way of rationalizing the electron delocalization, also gives the stabilization energy and the redistribution of electron density in bonding and antibonding orbitals. The *NBO* program (Version 3.1; Glendening *et al.*, 1998) was used for the NBO calculations, as implemented in the *GAUSSIAN03* package (Frisch *et al.*, 2004), on the optimized geometry of **1**. Equation (1) gives the stabilization energy $E(2)$ associated with the delocalization $i \rightarrow j$ for each donor (i) and acceptor (j):

$$E(2) = q_t \frac{(F_{ij})}{(E_j - E_i)} \qquad (1)$$

where q_i is the donor orbital occupancy, E_i and E_j are the diagonal, and F_{ij} is the orbital energy (off-diagonal elements of the Fock matrix) (Sebastian & Sundaraganesan, 2010). The larger values of $E(2)$ means that there are stronger interactions between electron donors and acceptors, and a more extensive conjugation of the whole system. Table 5 summarizes only the interactions where the stabilization energies are greater than 15 kcal mol^{-1}.

According to Table 5, the considerable stabilization energy values for **1** are in the range 15.75–59.66 kcal mol^{-1}. The observed strongest interaction was identified for the electron donation from the donor lone pair n1(N2) orbital to the π^*(C4—O1) antibonding orbital, with a 59.66 kcal mol^{-1} stabilization energy, which contributes to a resonance interaction in the amide group of the molecule. The other significant contributions in the second-order perturbation approach table for the compound are n1(N2)$\rightarrow\pi^*$(C3—N1), n2(S1)$\rightarrow\pi^*$(C3—N1), n2(O2)$\rightarrow\pi^*$(C7—C8) and n2(O2)$\rightarrow\pi^*$(C5—C6), with stabilization energies of 42.74, 30.93, 26.98 and 25.36 kcal mol^{-1}, respectively. NBO analysis of the compound reveals that the electron delocalization in the amide groups makes these groups more polar, and the O atom and N—H proton become much better hydrogen-bond acceptors and donors.

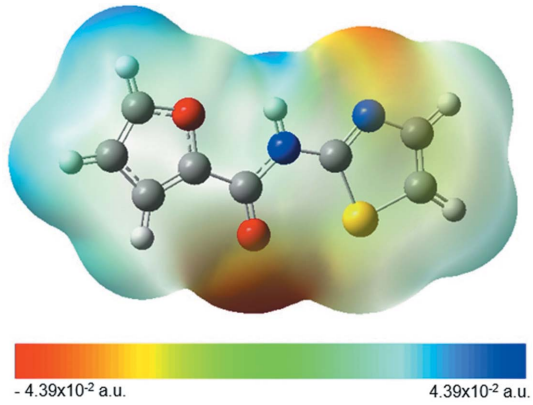

Figure 11
Molecular electrostatic potential (MEP) map of **1**.

3.6.2. Molecular electrostatic potential. The molecular electrostatic potential (MEP) map, which is related directly to electronic density, is very useful for understanding the sites for electrophilic and nucleophilic reactions, and also the hydrogen-bonding interactions of a molecule. An MEP represents different values of electrostatic potential with different colours (Murray & Sen, 1976). The most positive regions, which have the strongest attraction, are represented by blue and the most electronegative regions, which have the strongest repulsion, are red on these maps. Fig. 11 shows the MEP of **1**. The colour scale on the map shows the lower and upper limits of electrostatic potential and, according to calculations, the electrostatic potential is in the range between -4.39×10^{-2} and 4.39×10^{-2} a.u. While the most positive regions are localized on the H atom bonded to the N atom of the amide group and the H atoms of the furan ring, the most negative regions are on the C═O oxygen of the amide group and the N atom of the thiazole ring. These results are also in agreement with the results obtained from NBO data.

3.6.3. Second-order nonlinear optical (NLO) properties. We have calculated the linear polarizability (α) and the first-order hyperpolarizability (β) values of **1** with the help of DFT in order to understand if the compound is a good candidate for nonlinear optical studies. Molecules with good NLO responses are widely used in the design of new materials in communication, signal processing and optical interconnection technologies (Sajan *et al.*, 2005). Because of their larger NLO susceptibilities arising from π-electron cloud movement from donor to acceptor, organic molecules have been studied much more in this area.

The linear polarizability α and the first hyperpolarizability β have been calculated using Equations (2) and (3), respectively (Sajan *et al.*, 2006):

$$\alpha = \frac{1}{3}\left[\alpha_{xx} + \alpha_{yy} + \alpha_{zz}\right] \qquad (2)$$

$$\alpha = [(\beta_{xxx} + \beta_{xyy} + \beta_{xzz})^2 + (\beta_{yyy} + \beta_{xxy} + \beta_{yzz})^2 + (\beta_{zzz} + \beta_{xxz} + \beta_{yyz})^2] \qquad (3)$$

Table 7
The minimum inhibition concentrations (MIC's) of the tested molecules.

'NT' denotes not tested.

Sample	Minimum inhibition concentration (μg ml^{-1})							
	Gram-staining-positive			Gram-staining-negative			Fungi	
	B. subtilis	*S. aureus*	*E. faecalis*	*E. coli*	*K. pneumoniae*	*P. aeruginosa*	*A. niger*	*C. albicans*
N-(Thiazol-2-yl)furan-2-carboxamide	500	500	500	1000	750	1000	1000	1000
Amoxicillin	<2	>1000	>1000	32	>1000	>1000	NT	NT
Tetracycline	<2	8	8	<2	8	4	NT	NT
Ketoconazole	NT	NT	NT	NT	NT	NT	1	2

To obtain the components of polarizability and the first hyperpolarizability, a 'polar=ENONLY' input was used in *GAUSSIAN03* at the B3LYP/6-311G(d,p) level, as in all the computations of this work in the gas phase. The calculated α and β values are 20.692 Å^3 and 6.233 × 10^{-30} cm^5 e.s.u.$^{-1}$ for **1**. It is common to compare these values with the values for urea and the values of α and β using the B3LYP/6-31G(d) method are 3.831 Å^3 and 0.372 × 10^{-30} cm^5 e.s.u.$^{-1}$ (Sun *et al.*, 2009). Thus, α is 5.4 times greater than for urea and β is 16.7 times greater than for urea. These values are relatively high when compared to the literature (Koşar & Albayrak, 2011; Bragiel *et al.*, 2018) and point to **1** being a good candidate for use in nonlinear optical materials. The efficacy of such materials will depend on their conforming to other requirements, such as the absence of a center of symmetry for second-order effects in crystalline solids.

3.6.4. Thermodynamic properties. DFT-based vibrational frequency calculations provide detailed information about standard thermodynamic functions like enthalpy (H^0_m), entropy (S^0_m) and heat capacity ($C^0_{p/m}$). The functions have been generated from the vibrational frequency calculations in the temperature range 100–500 K for **1** in this study and are summarized in Table 6.

Fig. 12 presents the correlation graphs, showing the changes of statistical functions against temperature. It is plain to see that the thermodynamic functions enthalpy, entropy and heat capacity increase with increasing temperature as a result of the increasing intensities of molecular vibration.

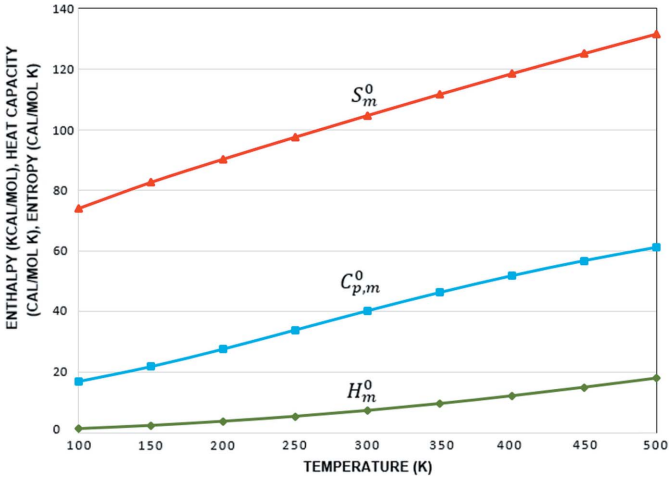

Figure 12
Thermodynamic functions *versus* temperature.

The following equations are the enthalpy, entropy and heat capacity functions for **1** in terms of temperature.

$$H^0_m = 0.0106 + 0.0071T - 6 \times 10^{-5}T^2, R^2 = 1 \quad (4)$$

$$S^0_m = 55.829 + 0.179T - 1.014 - 6 \times 10^{-5}T^2, R^2 = 0.9986 \quad (5)$$

$$C^0_m = -5.492 + 0.213T + 8.607 - 6 \times 10^{-5}T^2, R^2 = 0.9999 \quad (6)$$

The correlation equations can be used in future studies to obtain the change in the Gibbs free energy of the reaction during the interactions of **1** with another compound.

3.7. Antimicrobial activities

Compound **1** was tested *in vitro* for antimicrobial activity against three Gram-staining-positive bacteria, three Gram-staining-negative bacteria and two fungi strains. While the compound showed better antimicrobial activity against Gram-staining-positive *S. aureus* and *E. faecalis* than the amoxicillin standard, it showed a lower effect on *B. subtilis* than the amoxicillin and tetracycline standards. Moreover, the compound showed better activity against the Gram-staining-negative *K. pneumoniae* and *P. aeruginosa* compared to the reference amoxicillin. The compound showed lower antifungal activity against the two studied fungi than the ketoconazole standard. The minimum inhibitory concentration (MIC) was tested for the compound and the results are listed in Table 7.

Recent studies have shown that different types of compounds containing a thiazole ring exhibit significant antibacterial activity (Sarojini *et al.*, 2010; Bikobo *et al.*, 2017). Sarojini *et al.* (2010) synthesized five new compounds including thiazole rings and evaluated the antimicrobial activity of these compounds. The MIC values of the five new compounds against four fungal strains (*Aspergillus fumigatus*, *Aspergillus flavus*, *Penicillium marneffei* and *Trichophyton mentagrophytes*) and four bacterial strains (*Staphylococcus aureus*, *Escherichia coli*, *Klebsiella pneumoniae* and *Pseudomonas aeruginosa*) were determined. They concluded that one of the four new compounds tested showed good activity against all the microorganisms. Bikoba and co-workers studied the antimicrobial activity of 14 novel thiazole-ring-containing

compounds. They found that all the new compounds showed antibacterial and antifungal properties, and that these compounds exhibited better inhibitory activities against *S. aureus* than the reference drug spectinomycin (Bikobo *et al.*, 2017).

4. Conclusions

The title thiazole-based heterocyclic amide derivative was synthesized and characterized by FT–IR, ^{1}H NMR and ^{13}C NMR spectroscopy, X-ray diffraction and elemental analysis. The results of the X-ray studies showed that intra- and intermolecular hydrogen bonds, C—H$\cdots\pi$ interactions, π–π interactions and weak van der Waals interactions stabilized the crystal structure in the 3D network. The noncovalent interactions were also studied theoretically by Hirshfeld surface, NBO and MEP analyses. The calculated linear polarizability and first-order hyperpolarizability values of **1** pointed to its potential for use in nonlinear optical materials (other than the centric crystals of **1**).

This compound was also evaluated for its *in vitro* antimicrobial activity against eight microorganisms, consisting of three Gram-positive bacteria, three Gram-negative bacteria and two fungi strains. In general, amide derivatives bearing a thiazole scaffold have good antimicrobial activity. This can be explained by the nature of the amide compound and the presence of heteroatoms (sulfur and nitrogen) in the structure, which may lead to increased activity. The results showed that **1** has a remarkable activity against *S. aureus*, *E. faecalis*, *K. pneumoniae* and *P. aeruginosa*. In line with the findings in this article, we hope that microbial-derived biologically active molecular entities and their analogues can assist in the development of new therapeutic agents in medicine and industry.

Funding information

Funding for this research was provided by: Sinop University (project No. SHMYO-BAP 1901-17-25).

References

Araniciu, C., Pârvu, A. E., Palage, M. D., Oniga, S. D., Benedec, D., Oniga, I. & Oniga, O. (2014). *Molecules*, **19**, 9240–9256.
Becke, A. D. (1993). *J. Chem. Phys.* **98**, 5648–5652.
Bhaskara Reddy, M. V., Srinivasulu, D., Peddanna, K., Apparao, Ch. & Ramesh, P. (2015). *Synth. Commun.* **45**, 2592–2600.
Bikobo, D. S. N., Vodnar, D. C., Stana, A., Tiperciuc, B., Nastasă, C., Douchet, M. & Oniga, O. (2017). *J. Saudi Chem. Soc.* **21**, 861–868.
Borcea, A. M., Ionuţ, I., Crişan, O. & Oniga, O. (2021). *Molecules*, **26**, 624.
Bragiel, P., Radkowska, I., Belka, R., Marciniak, B. & Bak, Z. (2018). *J. Mol. Struct.* **1154**, 27–38.
Bruker (2013). *APEX3* and *SAINT*. Bruker AXS Inc., Madison, Wisconsin, USA.
Bueno, J. M., Carda, M., Crespo, B., Cuñat, A. C., de Cozar, C., León, M. L., Marco, J. A., Roda, N. & Sanz-Cervera, J. F. (2016). *Bioorg. Med. Chem. Lett.* **26**, 3938–3944.
Çakmak, Ş., Kütük, H., Odabaşoğlu, M., Yakan, H. & Büyükgüngör, O. (2016). *Lett. Org. Chem.* **13**, 181–194.
Chhabria, M. T., Patel, S., Modi, P. & Brahmkshatriya, P. S. (2016). *Curr. Top. Med. Chem.* **16**, 2841–2862.
Choi, M., Won, S.-W., Jo, H., Viji, M., Seo, S.-Y., Lee, Y.-J., Lee, H.-S., Lee, H., Hong, J. T., Kwak, Y.-S. & Jung, J.-K. (2014). *Tetrahedron Lett.* **55**, 6582–6584.
Demir, S., Çakmak, Ş., Dege, N., Kütük, H., Odabaşoğlu, M. & Kepekci, R. A. (2015). *J. Mol. Struct.* **1100**, 582–591.
Ditchfield, R., Hehre, W. J. & Pople, J. A. (1971). *J. Chem. Phys.* **54**, 724–728.
El-Enany, W. A. M. A., Gomha, S. M., El-Ziaty, A. K., Hussein, W., Abdulla, M. M., Hassan, S. A., Sallam, H. A. & Ali, R. S. (2020). *Synth. Commun.* **50**, 85–96.
Etter, M. C., MacDonald, J. C. & Bernstein, J. (1990). *Acta Cryst.* B**46**, 256–262.
Farrugia, L. J. (2012). *J. Appl. Cryst.* **45**, 849–854.
Frisch, M. J., *et al.* (2004). *GAUSSIAN03*. Gaussian Inc., Wallingford, CT, USA. https://gaussian.com/.
Gao, H., Liu, P., Yang, Y. & Gao, F. (2016). *RSC Adv.* **6**, 83438–83447.
Geronikaki, A. A., Pitta, E. P. & Liaras, K. S. (2013). *Curr. Med. Chem.* **20**, 4460–4480.
Glendening, E. D., Reed, A. E., Carpenter, J. E. & Weinhold, F. (1998). *NBO*. Version 3.1. Theoretical Chemistry Institute, University of Madison–Wisconsin, USA.
Gomha, S. M., Edrees, M. M. & Altalbawy, F. M. (2016). *Int. J. Mol. Sci.* **17**, 1499.
Hennig, L., Ayala-Leon, K., Angulo-Cornejo, J., Richter, R. & Beyer, L. (2009). *J. Fluor. Chem.* **130**, 453–460.
Iriarte, A. G., Erben, M. F., Gholivand, K., Jios, J. L., Ulic, S. E. & Della Védova, C. O. (2008). *J. Mol. Struct.* **886**, 66–71.
Jaishree, V., Ramdas, N., Sachin, J. & Ramesh, B. (2012). *J. Saudi Chem. Soc.* **16**, 371–376.
Kaur Gill, J. P., Sethi, N. & Mohan, A. (2018). *Orient. J. Chem.* **34**, 2378–2383.
Kerdphon, S., Quan, X., Parihar, V. S. & Andersson, P. G. (2015). *J. Org. Chem.* **80**, 11529–11537.
Koşar, B. & Albayrak, Ç. (2011). *Spectrochim. Acta A Mol. Biomol. Spectrosc.* **78**, 160–167.
Koşar Kırca, B. K., Çakmak, Ş., Kütük, H., Odabaşoğlu, M. & Büyükgüngör, O. (2018). *J. Mol. Struct.* **1151**, 191–197.
Koşar Kırca, B. K., Çakmak, Ş., Yakan, H., Odabaşoğlu, M., Büyükgüngör, O. & Kütük, H. (2020). *J. Mol. Struct.* **1203**, 127314.
Kumar, G. & Singh, N. P. (2021). *Bioorg. Chem.* **107**, 104608.
Lee, C., Yang, W. & Parr, R. G. (1988). *Phys. Rev. B*, **37**, 785–789.
Macrae, C. F., Sovago, I., Cottrell, S. J., Galek, P. T. A., McCabe, P., Pidcock, E., Platings, M., Shields, G. P., Stevens, J. S., Towler, M. & Wood, P. A. (2020). *J. Appl. Cryst.* **53**, 226–235.
Mazik, M., Bläser, D. & Boese, R. (1999). *Tetrahedron*, **55**, 12771–12782.
Meleddu, R., Distinto, S., Corona, A., Maccioni, E., Arridu, A., Melis, C., Bianco, G., Matyus, P., Cottiglia, F., Sanna, A. & De Logu, A. (2016). *J. Enzyme Inhib. Med. Chem.* **31**, 1672–1677.
Mishchenko, M., Shtrygol, S., Kaminskyy, D. & Lesyk, R. (2020). *Sci. Pharm.* **88**, 16.
Mishra, I., Mishra, R., Mujwar, S., Chandra, P. & Sachan, N. (2020). *J. Heterocycl. Chem.* **57**, 2304–2329.
Murray, J. S. & Sen, K. (1976). In *Molecular Electrostatic Potentials, Concepts and Applications*. Amsterdam: Elsevier.
Prabukanthan, P., Lakshmi, R., Harichandran, G. & Kumar, C. S. (2018). *J. Mol. Struct.* **1156**, 62–73.
Ramos-Inza, S., Aydillo, C., Sanmartín, C. & Plano, D. (2019). *Thiazole Moiety: An Interesting Scaffold for Developing New Antitumoral Compounds*, in *Heterocycles: Synthesis and Biological Activities*, edited by B. P. Nandeshwarappa & S. O Sadashiv, pp. 1–21. London: IntechOpen.
Rödl, C. B., Vogt, D., Kretschmer, S. B. M., Ihlefeld, K., Barzen, S., Brüggerhoff, A., Achenbach, J., Proschak, E., Steinhilber, D., Stark, H. & Hofmann, B. (2014). *Eur. J. Med. Chem.* **84**, 302–311.
Rubio-Pérez, L., Sharma, P., Pérez-Flores, F. J., Velasco, L., Arias, J. L. & Cabrera, A. (2012). *Tetrahedron*, **68**, 2342–2348.

Sajan, D., Joe, H., Jayakumar, V. S. & Zaleski, J. (2006). *J. Mol. Struct.* **785**, 43–53.
Sajan, D., Joe, I. H., Zaleski, J. & Jayakumar, V. S. (2005). *Laser Phys. Lett.* **2**, 343–350.
Sarojini, B. K., Krishna, B. G., Darshanraj, C. G., Bharath, B. R. & Manjunatha, H. (2010). *Eur. J. Med. Chem.* **45**, 3490–3496.
Schwalbe, R., Steele-Moore, L. & Goodwin, A. (2007). Editors. *Antimicrobial Susceptibility Testing Protocols*, p. 430. Boca Raton: CRC Press.
Sebastian, S. & Sundaraganesan, N. (2010). *Spectrochim. Acta A Mol. Biomol. Spectrosc.* **75**, 941–952.
Sharma, P. C., Bansal, K. K., Sharma, A., Sharma, D. & Deep, A. (2020). *Eur. J. Med. Chem.* **188**, 112016.
Sheldrick, G. M. (2008). *Acta Cryst.* A**64**, 112–122.
Sheldrick, G. M. (2015). *Acta Cryst.* C**71**, 3–8.
Shyamapada, S., Christoph, M. & Mitra, S. (2016). *ACSi*, **63**, 129–137.
Siddiqui, R., Akhter, S., Saify, Z. S., Haider, S., Ali, M. & Mallick, T. Z. (2019). *Pak. J. Pharm. Sci.* **32**, 2033–2039.
Sonar, V. N., Parkin, S. & Crooks, P. A. (2012). *Acta Cryst.* C**68**, o405–o407.
Spackman, M. A. & Jayatilaka, D. (2009). *CrystEngComm*, **11**, 19–32.
Spackman, P. R., Turner, M. J., McKinnon, J. J., Wolff, S. K., Grimwood, D. J., Jayatilaka, D. & Spackman, M. A. (2021). *CrystalExplorer*. Version 21.5. University of Western Australia. https://crystalexplorer.scb.uwa.edu.au/.
Srivastava, N., Kumar, A. & Mehrotra, A. (2019). *Indian J. Chem. B*, **58**, 1413–1415.
Sun, Y. X., Hao, Q. L., Wei, W. X., Yu, Z. X., Lu, L. D., Wang, X. & Wang, Y. S. (2009). *J. Mol. Struct. Theochem*, **904**, 74–82.
Tojiboev, A., Zhurakulov, S., Englert, U., Wang, R., Kalf, I., Vinogradova, V., Turgunov, K. & Tashkhodjaev, B. (2020). *Proceedings*, **62**, 1–9.
Venkatachalam, T. K., Sudbeck, E. A., Mao, C. & Uckun, F. M. (2001). *Bioorg. Med. Chem. Lett.* **11**, 523–528.
Wang, G., Peng, Z., Gong, Z. & Li, Y. (2018). *Bioorg. Chem.* **78**, 195–200.
Weng, J.-Q., Liu, X.-H. & Tong, G.-T. (2013). *Asian J. Chem.* **25**, 2149–2152.
Yakan, H., Cakmak, S., Kutuk, H., Yenigun, S. & Ozen, T. (2020). *Res. Chem. Intermed.* **46**, 2767–2787.

supporting information

Acta Cryst. (2022). C**78**, 201-211 [https://doi.org/10.1107/S2053229622002066]

Experimental and theoretical investigations on a furan-2-carboxamide-bearing thiazole: synthesis, molecular characterization by IR/NMR/XRD, electronic characterization by DFT, Hirshfeld surface analysis and biological activity

Şükriye Çakmak, Başak Koşar Kırca, Aysel Veyisoğlu, Hasan Yakan, Cem Cüneyt Ersanlı and Halil Kütük

Computing details

Data collection: *APEX3* (Bruker, 2013); cell refinement: *SAINT* (Bruker, 2013); data reduction: *SAINT* (Bruker, 2013); program(s) used to solve structure: *SHELXS2013* (Sheldrick, 2008); program(s) used to refine structure: *SHELXL2013* (Sheldrick, 2015); molecular graphics: *Mercury* (Macrae *et al.*, 2020); software used to prepare material for publication: *WinGX* (Farrugia, 2012).

N-(Thiazol-2-yl)furan-2-carboxamide

Crystal data

$C_8H_6N_2O_2S$
$M_r = 194.21$
Monoclinic, $P2_1/n$
$a = 11.9532$ (11) Å
$b = 11.1161$ (10) Å
$c = 13.4093$ (12) Å
$\beta = 104.071$ (3)°
$V = 1728.3$ (3) Å^3
$Z = 8$
$F(000) = 800$
$D_x = 1.493$ Mg m^{-3}
Mo $K\alpha$ radiation, $\lambda = 0.71073$ Å
Cell parameters from 9964 reflections
$\theta = 2.4$–28.2°
$\mu = 0.34$ mm^{-1}
$T = 296$ K
Block, colourless
0.17 × 0.12 × 0.11 mm

Data collection

Bruker APEXII CCD diffractometer
φ and ω scans
44822 measured reflections
4276 independent reflections
3424 reflections with $I > 2\sigma(I)$
$R_{int} = 0.035$
$\theta_{max} = 28.3°$, $\theta_{min} = 2.4°$
$h = -15\rightarrow15$
$k = -14\rightarrow14$
$l = -17\rightarrow17$

Refinement

Refinement on F^2
Least-squares matrix: full
$R[F^2 > 2\sigma(F^2)] = 0.045$
$wR(F^2) = 0.134$
$S = 0.94$
4276 reflections
241 parameters
0 restraints
Hydrogen site location: mixed
H atoms treated by a mixture of independent and constrained refinement
$w = 1/[\sigma^2(F_o^2) + (0.0677P)^2 + 1.5631P]$ where $P = (F_o^2 + 2F_c^2)/3$
$(\Delta/\sigma)_{max} < 0.001$
$\Delta\rho_{max} = 0.41$ e Å^{-3}
$\Delta\rho_{min} = -0.33$ e Å^{-3}

Special details

Geometry. All esds (except the esd in the dihedral angle between two l.s. planes) are estimated using the full covariance matrix. The cell esds are taken into account individually in the estimation of esds in distances, angles and torsion angles; correlations between esds in cell parameters are only used when they are defined by crystal symmetry. An approximate (isotropic) treatment of cell esds is used for estimating esds involving l.s. planes.

Refinement. A suitable sample of size 0.17 × 0.312 × 0.11 mm was chosen for the single crystal X-ray study. Reflections were collected in the rotation mode (ω scanning mode) and cell parameters were determined using the X-AREA software (Stoe & Cie, 2002). Absorption correction (μ = 0.339 mm^{-1}) was carried out using the X-RED32 software (Stoe & Cie, 2002). The structure was solved by direct methods using SHELXS2013 (Sheldrick, 2008). The refinement was carried out by full-matrix least-squares method using SHELXL2013 on the positional and anisotropic temperature parameters of the non-H atoms, or equivalently corresponding to 241 crystallographic parameters (Sheldrick, 2015). Under the condition of the I > 2σ(I) threshold, the structure was refined to R = 0.045, wR2 = 0.109, S = 0.941 with 3424 observed reflections. The other data collection conditions and parameters of refinement process are listed in Table 1.

Fractional atomic coordinates and isotropic or equivalent isotropic displacement parameters (Å^2)

	x	*y*	*z*	U_{iso}*/U_{eq}
C1	0.2190 (2)	0.6474 (2)	0.2453 (2)	0.0499 (6)
H1	0.1624	0.7060	0.2258	0.060*
C2	0.2906 (2)	0.6111 (2)	0.18791 (19)	0.0470 (5)
H2	0.2877	0.6433	0.1233	0.056*
C3	0.35429 (16)	0.49271 (16)	0.32135 (15)	0.0321 (4)
C4	0.40753 (17)	0.37067 (18)	0.47478 (16)	0.0356 (4)
C5	0.47912 (17)	0.27130 (19)	0.52414 (15)	0.0362 (4)
C6	0.4940 (2)	0.2238 (2)	0.61889 (18)	0.0490 (6)
H6	0.4588	0.2490	0.6700	0.059*
C7	0.5732 (2)	0.1285 (2)	0.62552 (19)	0.0533 (6)
H7	0.6004	0.0787	0.6819	0.064*
C8	0.6017 (2)	0.1233 (2)	0.5352 (2)	0.0516 (6)
H8	0.6528	0.0681	0.5186	0.062*
C9	0.6672 (2)	0.1397 (2)	0.19249 (18)	0.0470 (5)
H9	0.7005	0.0644	0.1902	0.056*
C10	0.5916 (2)	0.1662 (2)	0.24828 (18)	0.0455 (5)
H10	0.5674	0.1093	0.2893	0.055*
C11	0.59902 (16)	0.34353 (18)	0.17865 (15)	0.0333 (4)
C12	0.62594 (18)	0.53124 (19)	0.09742 (16)	0.0381 (4)
C13	0.59577 (19)	0.65833 (19)	0.08489 (16)	0.0391 (5)
C14	0.6377 (3)	0.7464 (2)	0.0358 (3)	0.0649 (8)
H14	0.6924	0.7379	−0.0025	0.078*
C15	0.5835 (3)	0.8537 (2)	0.0531 (2)	0.0609 (7)
H15	0.5956	0.9299	0.0291	0.073*
C16	0.5120 (3)	0.8244 (2)	0.1101 (2)	0.0694 (8)
H16	0.4643	0.8787	0.1327	0.083*
N1	0.36863 (15)	0.52284 (16)	0.23117 (14)	0.0400 (4)
N3	0.55182 (16)	0.28347 (16)	0.24137 (14)	0.0413 (4)
O1	0.33984 (15)	0.42142 (15)	0.51616 (13)	0.0518 (4)
O2	0.54529 (14)	0.21034 (15)	0.47094 (12)	0.0468 (4)
O3	0.69889 (17)	0.48864 (16)	0.05720 (15)	0.0621 (5)
O4	0.51695 (18)	0.70450 (15)	0.13144 (14)	0.0587 (5)

S1	0.24661 (5)	0.57033 (5)	0.36007 (5)	0.04299 (16)
S2	0.69414 (5)	0.26387 (5)	0.12559 (5)	0.04722 (17)
N2	0.41974 (15)	0.40403 (15)	0.37949 (13)	0.0339 (4)
H2A	0.465 (2)	0.369 (2)	0.3532 (18)	0.041*
N4	0.57260 (15)	0.46326 (15)	0.15663 (14)	0.0361 (4)
H4	0.521 (2)	0.490 (2)	0.1791 (18)	0.043*

Atomic displacement parameters (Å²)

	U^{11}	U^{22}	U^{33}	U^{12}	U^{13}	U^{23}
C1	0.0454 (12)	0.0394 (11)	0.0671 (15)	0.0115 (10)	0.0177 (11)	0.0092 (11)
C2	0.0462 (12)	0.0440 (12)	0.0531 (13)	0.0074 (10)	0.0167 (10)	0.0124 (10)
C3	0.0323 (9)	0.0266 (9)	0.0410 (10)	−0.0028 (7)	0.0160 (8)	−0.0047 (8)
C4	0.0369 (10)	0.0351 (10)	0.0377 (10)	−0.0059 (8)	0.0143 (8)	−0.0040 (8)
C5	0.0342 (10)	0.0393 (11)	0.0373 (10)	−0.0033 (8)	0.0133 (8)	−0.0019 (8)
C6	0.0463 (12)	0.0627 (15)	0.0406 (12)	0.0050 (11)	0.0160 (10)	0.0069 (11)
C7	0.0517 (14)	0.0583 (15)	0.0492 (13)	0.0073 (11)	0.0109 (11)	0.0151 (11)
C8	0.0507 (13)	0.0467 (13)	0.0597 (15)	0.0101 (10)	0.0175 (11)	0.0069 (11)
C9	0.0536 (13)	0.0364 (11)	0.0503 (13)	0.0112 (10)	0.0110 (10)	−0.0036 (9)
C10	0.0568 (13)	0.0338 (11)	0.0483 (13)	0.0064 (10)	0.0172 (10)	0.0061 (9)
C11	0.0333 (9)	0.0341 (10)	0.0347 (10)	0.0001 (7)	0.0126 (8)	−0.0014 (8)
C12	0.0426 (11)	0.0384 (11)	0.0377 (10)	−0.0048 (8)	0.0181 (9)	0.0008 (8)
C13	0.0442 (11)	0.0393 (11)	0.0367 (10)	−0.0024 (9)	0.0156 (9)	0.0035 (8)
C14	0.0711 (18)	0.0509 (14)	0.087 (2)	0.0061 (13)	0.0467 (16)	0.0243 (14)
C15	0.0783 (19)	0.0411 (13)	0.0668 (17)	0.0022 (12)	0.0244 (14)	0.0167 (12)
C16	0.110 (2)	0.0410 (13)	0.0704 (18)	0.0182 (15)	0.0463 (18)	0.0074 (12)
N1	0.0407 (9)	0.0392 (9)	0.0444 (10)	0.0059 (7)	0.0190 (8)	0.0051 (8)
N3	0.0495 (10)	0.0334 (9)	0.0468 (10)	0.0048 (7)	0.0231 (8)	0.0056 (8)
O1	0.0610 (10)	0.0554 (10)	0.0484 (9)	0.0130 (8)	0.0314 (8)	0.0036 (8)
O2	0.0557 (9)	0.0468 (9)	0.0438 (8)	0.0104 (7)	0.0234 (7)	0.0034 (7)
O3	0.0748 (12)	0.0491 (10)	0.0827 (13)	0.0055 (9)	0.0581 (11)	0.0093 (9)
O4	0.0855 (13)	0.0411 (9)	0.0653 (11)	0.0094 (9)	0.0492 (10)	0.0093 (8)
S1	0.0430 (3)	0.0376 (3)	0.0552 (3)	0.0064 (2)	0.0250 (2)	−0.0036 (2)
S2	0.0493 (3)	0.0451 (3)	0.0551 (4)	0.0086 (2)	0.0279 (3)	−0.0030 (2)
N2	0.0361 (8)	0.0318 (8)	0.0381 (9)	0.0022 (7)	0.0175 (7)	−0.0006 (7)
N4	0.0392 (9)	0.0326 (8)	0.0432 (9)	0.0019 (7)	0.0226 (8)	0.0021 (7)

Geometric parameters (Å, º)

C1—C2	1.344 (3)	C9—S2	1.719 (3)
C1—S1	1.721 (3)	C9—H9	0.9300
C1—H1	0.9300	C10—N3	1.383 (3)
C2—N1	1.381 (3)	C10—H10	0.9300
C2—H2	0.9300	C11—N3	1.305 (2)
C3—N1	1.306 (3)	C11—N4	1.383 (3)
C3—N2	1.377 (3)	C11—S2	1.7252 (19)
C3—S1	1.7308 (18)	C12—O3	1.226 (3)
C4—O1	1.224 (2)	C12—N4	1.362 (2)

C4—N2	1.372 (3)	C12—C13	1.458 (3)
C4—C5	1.454 (3)	C13—C14	1.342 (3)
C5—C6	1.347 (3)	C13—O4	1.352 (3)
C5—O2	1.367 (2)	C14—C15	1.403 (4)
C6—C7	1.409 (4)	C14—H14	0.9300
C6—H6	0.9300	C15—C16	1.318 (4)
C7—C8	1.337 (4)	C15—H15	0.9300
C7—H7	0.9300	C16—O4	1.362 (3)
C8—O2	1.360 (3)	C16—H16	0.9300
C8—H8	0.9300	N2—H2A	0.81 (2)
C9—C10	1.339 (3)	N4—H4	0.80 (3)

C2—C1—S1	110.64 (17)	N3—C11—N4	121.20 (17)
C2—C1—H1	124.7	N3—C11—S2	115.77 (15)
S1—C1—H1	124.7	N4—C11—S2	123.03 (14)
C1—C2—N1	115.6 (2)	O3—C12—N4	121.7 (2)
C1—C2—H2	122.2	O3—C12—C13	120.40 (19)
N1—C2—H2	122.2	N4—C12—C13	117.86 (18)
N1—C3—N2	121.58 (17)	C14—C13—O4	109.5 (2)
N1—C3—S1	115.13 (15)	C14—C13—C12	130.7 (2)
N2—C3—S1	123.28 (14)	O4—C13—C12	119.70 (18)
O1—C4—N2	121.9 (2)	C13—C14—C15	107.3 (2)
O1—C4—C5	121.62 (19)	C13—C14—H14	126.4
N2—C4—C5	116.43 (17)	C15—C14—H14	126.4
C6—C5—O2	109.72 (19)	C16—C15—C14	106.0 (2)
C6—C5—C4	130.9 (2)	C16—C15—H15	127.0
O2—C5—C4	119.35 (17)	C14—C15—H15	127.0
C5—C6—C7	106.7 (2)	C15—C16—O4	111.2 (2)
C5—C6—H6	126.7	C15—C16—H16	124.4
C7—C6—H6	126.7	O4—C16—H16	124.4
C8—C7—C6	106.9 (2)	C3—N1—C2	110.11 (18)
C8—C7—H7	126.6	C11—N3—C10	109.25 (18)
C6—C7—H7	126.6	C8—O2—C5	106.43 (17)
C7—C8—O2	110.3 (2)	C13—O4—C16	105.90 (19)
C7—C8—H8	124.8	C1—S1—C3	88.55 (10)
O2—C8—H8	124.8	C9—S2—C11	88.36 (10)
C10—C9—S2	110.59 (17)	C4—N2—C3	123.13 (17)
C10—C9—H9	124.7	C4—N2—H2A	120.5 (17)
S2—C9—H9	124.7	C3—N2—H2A	116.3 (17)
C9—C10—N3	116.0 (2)	C12—N4—C11	122.93 (17)
C9—C10—H10	122.0	C12—N4—H4	121.6 (18)
N3—C10—H10	122.0	C11—N4—H4	115.4 (18)

S1—C1—C2—N1	0.0 (3)	S2—C11—N3—C10	−0.5 (2)
O1—C4—C5—C6	−5.9 (4)	C9—C10—N3—C11	0.3 (3)
N2—C4—C5—C6	174.3 (2)	C7—C8—O2—C5	−0.2 (3)
O1—C4—C5—O2	173.91 (19)	C6—C5—O2—C8	0.1 (3)
N2—C4—C5—O2	−5.9 (3)	C4—C5—O2—C8	−179.74 (19)

O2—C5—C6—C7	0.0 (3)	C14—C13—O4—C16	−0.4 (3)
C4—C5—C6—C7	179.8 (2)	C12—C13—O4—C16	176.9 (2)
C5—C6—C7—C8	−0.1 (3)	C15—C16—O4—C13	0.0 (4)
C6—C7—C8—O2	0.2 (3)	C2—C1—S1—C3	−0.3 (2)
S2—C9—C10—N3	0.0 (3)	N1—C3—S1—C1	0.56 (17)
O3—C12—C13—C14	−2.0 (4)	N2—C3—S1—C1	−178.42 (18)
N4—C12—C13—C14	176.5 (3)	C10—C9—S2—C11	−0.25 (19)
O3—C12—C13—O4	−178.6 (2)	N3—C11—S2—C9	0.47 (18)
N4—C12—C13—O4	−0.1 (3)	N4—C11—S2—C9	−179.10 (19)
O4—C13—C14—C15	0.6 (3)	O1—C4—N2—C3	−2.8 (3)
C12—C13—C14—C15	−176.3 (2)	C5—C4—N2—C3	176.97 (18)
C13—C14—C15—C16	−0.6 (4)	N1—C3—N2—C4	179.55 (19)
C14—C15—C16—O4	0.4 (4)	S1—C3—N2—C4	−1.5 (3)
N2—C3—N1—C2	178.33 (19)	O3—C12—N4—C11	2.3 (3)
S1—C3—N1—C2	−0.7 (2)	C13—C12—N4—C11	−176.26 (19)
C1—C2—N1—C3	0.4 (3)	N3—C11—N4—C12	175.2 (2)
N4—C11—N3—C10	179.04 (19)	S2—C11—N4—C12	−5.2 (3)

Hydrogen-bond geometry (Å, º)

D—H···*A*	*D*—H	H···*A*	*D*···*A*	*D*—H···*A*
C8—H8···O3^{i}	0.93	2.42	3.301 (3)	159
N2—H2*A*···N3	0.81 (2)	2.23 (3)	3.023 (2)	164 (2)
N4—H4···N1	0.80 (3)	2.14 (3)	2.927 (2)	168 (2)

Symmetry code: (i) −*x*+3/2, *y*−1/2, −*z*+1/2.